Journal of Alloys and Compounds 509 (2011) 8804–8811

Contents lists available at ScienceDirect

Journal of Alloys and Compounds

journal homepage: www.elsevier.com/locate/jallcom

Effect of MnO doping on the structure, microstructure and electrical properties of the (K,Na,Li)(Nb,Ta,Sb)O_3 lead-free piezoceramics

F. Rubio-Marcos [a,*], P. Marchet [a], X. Vendrell [b], J.J. Romero [c], F. Rémondière [a], L. Mestres [b], J.F. Fernández [c]

[a] Laboratoire de Science des Procédés Céramiques et de Traitements de Surface, UMR 6638 CNRS, Université de Limoges, Centre Européen de la Céramique, 12, rue Atlantis, 87068 Limoges Cedex, France
[b] Grup de Química de l'Estat Sòlid, Departament de Química Inorgànica, Universitat de Barcelona, 08028 Barcelona, Spain
[c] Electroceramic Department, Instituto de Cerámica y Vidrio, CSIC, Kelsen 5, 28049 Madrid, Spain

ARTICLE INFO

Article history:
Received 7 April 2011
Received in revised form 13 June 2011
Accepted 17 June 2011
Available online 23 June 2011

Keywords:
Ferroelectrics
Solid state reaction
Piezoelectricity
X-ray diffraction

ABSTRACT

Mn^{2+}-doped (K,Na,Li)(Nb,Ta,Sb)O_3 lead-free piezoelectric ceramics have been prepared by a conventional sintering technique. The effects of Mn^{2+} doping on the phase structure, microstructure and ferro-piezoelectric properties of the ceramics have been evaluated. MnO doping modifies the (K,Na,Li)(Nb,Ta,Sb)O_3 structure, giving rise to the appearance of a TTB-like secondary phase and to changes on the orthorhombic to tetragonal phase transition temperature. The modification of this temperature induces a reduction of the piezoelectric constants, which is accompanied by an increase on the mechanical quality factor. Mn^{2+} ions incorporate into the perovskite structure in different off ways depending on their concentration.

1. Introduction

Lead zirconate-titanate ceramics (PZT) are the most widely used piezoelectric materials to date, on account of their high piezoelectric response, large scale production capability and the tailoring of their properties through composition. Recently, the European Union has published a directive (RoHS) [1] avoiding the use of lead because of its toxicity and environmental risks. Nevertheless, PZT ceramics are temporarily tolerated because of the lack of an industrially adequate alternative. Among the available lead-free ferroelectric materials under study, one promising candidate on account of its good electromechanical properties is the family of sodium potassium niobate (K,Na)NbO_3 (KNN) [2]. As for PZT, the sinterability of KNN materials can be improved by using different sintering aids, such as CuO [3,4], SnO_2 [5], ZnO [6] and MnO [7]. These chemical elements usually enter in B position of the ABO_3 perovskite structure and thus produce A-site vacancies that suppress the formation of the hygroscopic secondary products [8]. Some studies have also been carried out concerning the formation of solid solutions, such as KNN–$SrTiO_3$ [9], KNN–$LiNbO_3$ [10], KNN–$LiTaO_3$ [11–13], KNN–$LiSbO_3$ [14] and KNN–$LiSbO_3$–$LiTaO_3$ [15,16].

Recently, the complex solid solution (K,Na,Li)(Nb,Ta,Sb)O_3 has revealed excellent piezoelectric properties [17], representing then a serious candidate for the substitution of PZT. Nevertheless, there are still some structural and electrical aspects that remain controversial with respect to the role of dopants in this system.

In a previous study concerning the (K,Na,Li)(Nb,Ta,Sb)O_3 compounds (abbreviated as KNL–NTS), we have demonstrated that the dielectric, piezoelectric and elastic properties of the material are fundamentally related to extrinsic effects [18]. The dielectric and mechanical losses at room temperature are similar to those of a soft PZT ceramic and too high to be used in power devices. Doping with suitable elements should be a way of minimizing the temperature sensitivity, reducing the dielectric losses, and enhancing mechanical quality factor. Therefore, in the present work, MnO was selected as the dopant of KNL–NTS ceramics. In view of its ionic radius ($r_{Mn^{2+}}$: 0.83 Å for a coordination number CN = 6 [19]), Mn^{2+} falls between the size range of B-site position ($r_{Nb^{5+}}$: 0.64 Å, $r_{Ta^{5+}}$: 0.64 Å, $r_{Sb^{5+}}$: 0.60 Å, CN = 6) and A-site (r_{K^+}: 1.64 Å, r_{Na^+}: 1.39 Å, r_{Li^+}: 0.90 Å, CN = 12). Thus, on the basis of ionic radii, the Mn^{2+} ion could substitute in either A or B-sites, the most probable position being the B-site according to crystal-chemistry considerations. Considering its valency, Mn^{2+} can either act as a donor-dopant if introduced in A-site or as an acceptor-dopant in B-site. Therefore, in order to introduce the Mn^{2+} ion into the A-site of the perovskite lattice, we selected A-site deficiency, with a global formula $(K_{0.44}Na_{0.52}Li_{0.04})_{(1-x)}Mn_{(x/2)}(Nb_{0.86}Ta_{0.10}Sb_{0.04})O_3$.

* Corresponding author. Tel.: +33 5 87 50 23 77; fax: +33 5 87 50 23 07.
E-mail address: fernando.rubio-marcos@unilim.fr (F. Rubio-Marcos).

0925-8388/$ – see front matter © 2011 Elsevier B.V. All rights reserved.
doi:10.1016/j.jallcom.2011.06.080

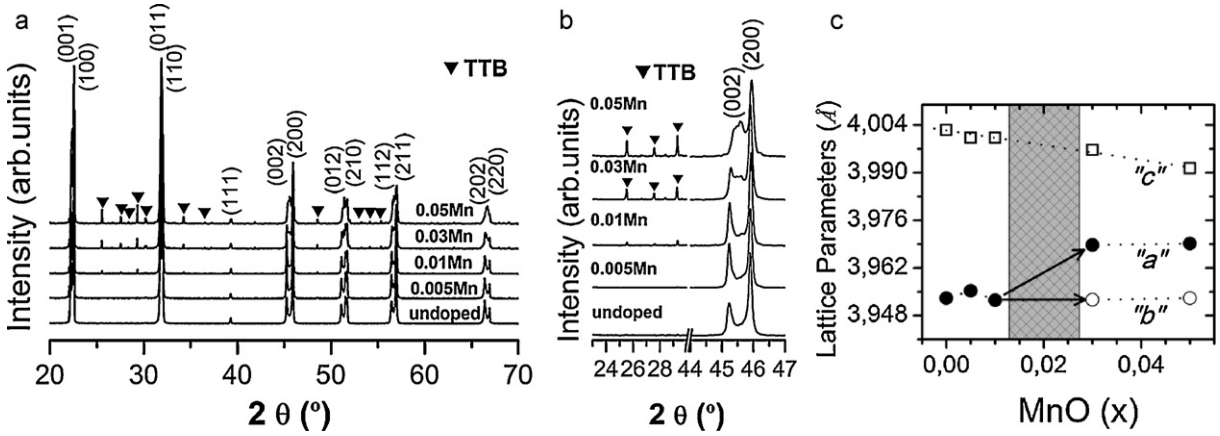

Fig. 1. (a) XRD patterns corresponding to the $(KNL)_{1-x}Mn_{x/2}$–NTS ceramics sintered at 1125 °C for 16 h. (b) Magnified XRD diffraction patterns in the 2θ range 23.5–29° and 44–47° of the $(KNL)_{1-x}Mn_{x/2}$–NTS ceramics. (c) Variation of lattice parameters of the $(KNL)_{1-x}Mn_{x/2}$–NTS ceramics as a function of the MnO content.

The effects of such MnO substitution on the phase composition, microstructure, dielectric and piezoelectric properties of $[(K_{0.44}Na_{0.52}Li_{0.04})_{1-x}Mn_{x/2}](Nb_{0.86}Ta_{0.10}Sb_{0.04})O_3$ ceramics were investigated. The MnO modification mechanisms on the piezoelectric, ferroelectric and dielectric properties of these ceramics were also discussed.

2. Experimental

The $[(K_{0.44}Na_{0.52}Li_{0.04})_{1-x}Mn_{x/2}](Nb_{0.86}Ta_{0.10}Sb_{0.04})O_3$ compositions with $x = 0.000, 0.005, 0.010, 0.030$ and 0.050, hereafter abbreviated as $(KNL)_{1-x}Mn_{x/2}$–NTS, were synthesized by conventional solid-state reaction [20]. The raw materials of analytical grade used in this study were K_2CO_3, Na_2CO_3, Li_2CO_3, MnO, Nb_2O_5, Ta_2O_5 and Sb_2O_5. These powders were weighed and mixed by attrition-milling using ZrO_2 balls in absolute ethanol medium for 3 h, dried and calcined at 700 °C for 2 h. The obtained materials were composed of particles with narrow size distribution of ~350 nm, formed by agglomerated nanometer-sized particles. The calcined powders were attrition milled again and cold-isostatically pressed at 200 MPa into discs of 10 mm in diameter and 0.7 mm in thickness. The pellets were finally sintered in air at 1125 °C for 16 h. The density of the sintered samples was measured using the Archimedes' method. All the obtained ceramics showed relative densities over 95% of the theoretical one. The relative densities were calculated from the XRD patterns of the ceramics.

The structural evolution produced by Mn^{2+} addition on the perovskite structure was followed by X-ray powder diffraction XRD (Siemens D5000, CuKα radiation). The lattice parameters were refined by a global simulation of the full diagram (pattern matching, *fullprof* program).

Microstructure was evaluated on polished and thermally etched samples (1000 °C for 5 min) using a Field Emission Scanning Electron Microscope, FE-SEM (Hitachi S-4700, Tokyo, Japan), equipped with Energy Dispersive Spectroscopy (EDS). The average grain size was determined from FE-SEM micrographs by an image processing and analysis program (Leica Qwin, Leica Microsystems Ltd., Cambridge, England) considering more than 500 grains in each measurement.

Electrical characterization was carried out on ceramic discs with fired silver paste (700 °C) on both sides as electrodes. The temperature dependence of the dielectric permittivity was measured using an impedance analyzer (HP4294A, Agilent Technologies Inc., Santa Clara, CA) in the frequency range of 100 Hz to 1 MHz and the temperature range of 30–600 °C, at 2 °C/min.

Piezoelectric properties were evaluated, after a poling process. This one was carried out in a silicone oil bath at 25 °C under a DC electric field of 40 kV/cm during 30 min. The piezoelectric constant d_{33} was measured using a piezo-d_{33} meter (YE2730A d_{33} METER, APC International). The piezoelectric constant d_{31} was determined at room temperature by the resonance/antiresonance method on the basis of IEEE standards. The planar mechanical quality factor, Q_m, which is related to the sharpness of the resonance frequency, was calculated using the following equation described in Ref. [21]:

$$Q_m = \frac{f_a^2}{2\pi f_r Z_m C^T (f_a^2 - f_r^2)} \quad (1)$$

where f_r (Hz) is the resonance frequency, f_a (Hz) is the antiresonance frequency, Z_m (ohm) is the minimum impedance at f_r and C^T (F) is the mechanically free capacitance at 1 kHz. Finally, the ferroelectric nature of the ceramics was determined using a hysteresis meter (RT 6000 HVS, RADIANT Technologies).

3. Results and discussion

3.1. Structural characterization

Fig. 1a displays the XRD patterns of the ceramics with different MnO amounts. In addition to the perovskite structure, a secondary phase was detected in samples with MnO content higher than 0.005. This secondary phase could be assigned to $K_3LiNb_6O_{17}$ [22] (KLN) or $K_6Nb_{10.88}O_{30}$ (PDF#87-1856), both with tetragonal tungsten-bronze type structure (TTB). Pornsuda Bomlai et al. also reported that a secondary phase with tungsten bronze structure is observed in MnO-doped $(Na_{0.5}K_{0.5}NbO_3)$–$(LiTaO_3)$ ceramics [7], while Feng et al. have also observed this secondary phase on KNN-based ceramics [23]. Fig. 1b shows a magnification of the 23.5–29.0° 2θ range, where the most intense diffraction peaks of the TTB secondary phase can be clearly observed. The XRD data reveal an increase of the TTB-type phase with the MnO content, without modification of its structure. For Li/Ta-modified KNN materials, the occurrence of this secondary phase was attributed to the volatilization and segregation of the alkali elements during sintering [24]. As a consequence, the TTB phase probably occurs here because of the A-site deficiency introduced by our choice of composition, a deficiency that increases with the Mn concentration.

Moreover, as represented in Fig. 1b, the MnO doping has an important impact on the perovskite structure. Indeed, the splitting of the (2 0 0) pseudo-cubic peak is strongly affected by MnO doping: for undoped material ($x = 0.00$), the splitting into (2 0 0) and (0 0 2) suggests a tetragonal symmetry, whereas for higher MnO content ($x \geq 0.03$), three peaks are needed in order to correctly fit the XRD data, suggesting then orthorhombic symmetry. In order to further analyze the effect of MnO doping on the crystalline structure, the lattice parameters were calculated. Thus, considering the aforementioned observations, the refinement of the lattice parameters was performed using a tetragonal unit-cell (space group P*4mm*) for compositions with $x < 0.03$, and an orthorhombic unit-cell (space group P*222*) for compositions with $x \geq 0.03$. Fig. 1c shows the variation of the lattice parameters as a function of the MnO amount. The intermediate state around $x \sim 0.02$, shadowed in this figure, corresponds to the transitional region. For low MnO contents (the tetragonal symmetry range), the "*a*" lattice parameters do not vary, suggesting that the Mn^{2+}-addition does not drastically modify the crystal structure. For higher MnO content ($x \geq 0.03$, orthorhombic range), "*a*" and "*b*" are different and increase with Mn addition. The parameter "*c*" decreases monotonously with MnO amount. To sum up, with increasing MnO content we observe both the appearance of the TTB secondary phase and the transformation of the perovskite structure from tetragonal to orthorhombic symmetry. Recently,

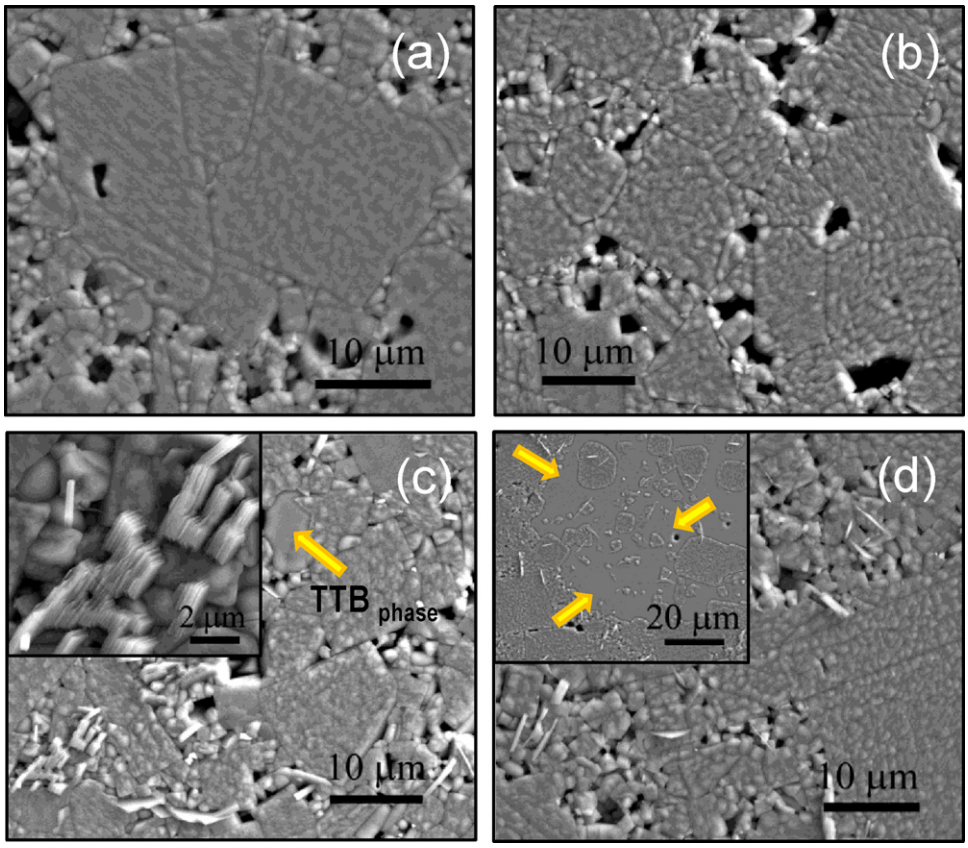

Fig. 2. Microstructure of polished and thermally etched surfaces of the $(KNL)_{1-x}Mn_{x/2}$–NTS ceramics sintered at 1125 °C for 16 h. (a) $x = 0.005$, (b) $x = 0.010$, (c) $x = 0.030$, and (d) $x = 0.050$. The insets of (c and d) show the presence of the secondary re-crystallizations in grain boundaries and grains with TTB structure, respectively.

it has been reported that MnO acts as a sintering aid in related $(Na_{1-x}K_x)(Nb_{1-y}Sb_y)O_3$ ceramics, but MnO was thought to not significantly affect the crystal structure [25]. By contrast, other authors [7] and the present XRD data for the $(KNL)_{1-x}Mn_{x/2}$–NTS composition suggest that substitution of Mn^{2+} ions in the perovskite lattice occurs and affects phase stability. This evolution clearly depends on the MnO content. For low x values ($x \leq 0.005$), the TTB phase is not observed and the perovskite structure with tetragonal symmetry apparently remains unchanged. For higher Mn contents ($x \geq 0.03$), the TTB phase is clearly present and its quantity increases with Mn^{2+} content. A structural evolution of the modified KNN phase is also observed, from a tetragonal to an orthorhombic unit-cell. The composition with $x = 0.01$ corresponds to an "intermediate" case where the TTB phase starts to nucleate (see Fig. 1b) but where the tetragonal symmetry of the perovskite structure seems to be maintained.

3.2. Microstructural characterization

The FE-SEM micrographs of the $(KNL)_{1-x}Mn_{x/2}$–NTS ceramics with x between 0.005 and 0.050 are shown in Fig. 2a–d. The FE-SEM micrographs show the $(KNL)_{1-x}Mn_{x/2}$–NTS morphology consisting on faceted grains and cube-shaped grains. The microstructure of the samples without MnO shows equiaxed grains and some large abnormal square or rectangular grains [6,20] (not shown in this work). A change of average grain size and grain morphology is observed with increasing MnO content, as depicted in Fig. 2a–d; the average grain size increases from ~1.5 μm in undoped ceramics [6,20] to ~8 μm for the higher MnO content, $x = 0.05$. Additionally, in all cases the microstructure of the system exhibits a bimodal grain size distribution. The bimodality of the system is significantly more marked for high values of x ($x \geq 0.03$) and may be attributed to the exaggerated grain growth process. This behaviour can be also observed in compositions with low MnO content, where coexists a high population of the small grains, size ~ 1.5 μm, and lower population of the abnormal grains, size > 10 μm. In addition, for highest MnO content ($x \geq 0.03$) secondary re-crystallization begins to appear in grain boundaries, see inset in Fig. 2c.

According to the literature [20], the densification of KNN-modified ceramics proceeds through formation of a liquid phase. This one contributes to sintering by accelerating particle redistribution on account of enhanced atomic mobility [26] and therefore, the general grain growth observed in doped samples is also believed to be a result of this liquid phase. Furthermore, the exaggerated grain growth process is driven by the difference in surface free energies between the advancing plane of large grains and the fine matrix grains. The presence of a liquid phase excess, especially in the ceramics with MnO content ≥ 0.03, facilitates and accelerates the kinetic of this process, producing more relevant bimodal grain size distribution. In addition in these samples, the grain morphology changed from sharp-cornered cubical grains with smooth surfaces to cut-cornered grains with rough surfaces, Fig. 2d, as it was reported by other authors in CuO-doped KNN-based ceramics [27].

As it has been discussed above, when increasing MnO content, the samples also show grains with a different morphology from that of the normal KNL–NTS and abnormal grains, marked with arrows in Fig. 2c and d. This phenomenon was more relevant when the MnO content increases. The energy dispersion spectrum analysis (EDS) reveals that the atomic percentages of elements change within the different grain regions, as previously reported for KNN and other systems [26]. Table 1 lists the compositions measured by EDS for the $x = 0.05$ sample at the locations marked in Fig. 3a. The results show clear differences between the different points, indicating a significant compositional segregation in the ceramics. The grain

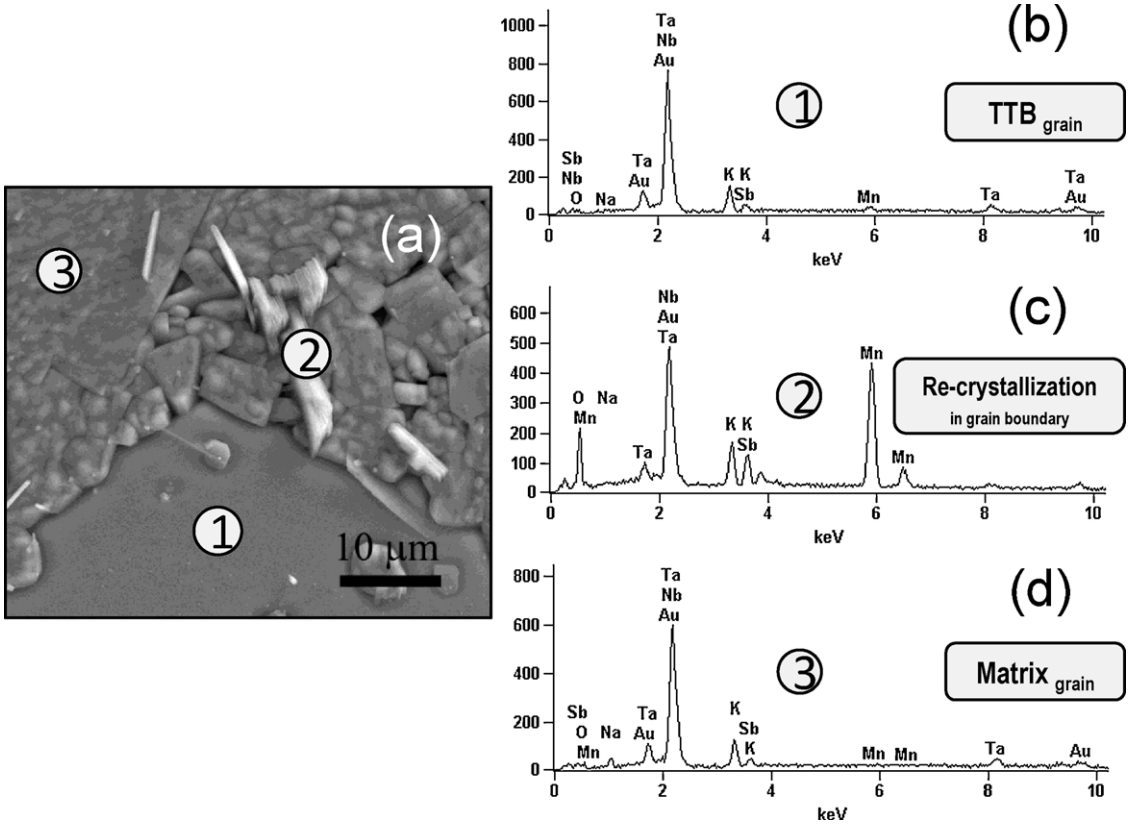

Fig. 3. (a) Microphotographs of the $(KNL)_{1-x}Mn_{x/2}$–NTS ceramics with the higher MnO addition, $x = 0.05$. On figure, the presence of a grain with TTB structure, the secondary re-crystallizations in grain boundaries and a grain with nominal composition are signalled with the points 1, 2 and 3, respectively. In the part (b) EDS spectra of a TTB grain (c) a secondary re-crystallization in grain boundaries and (d) a matrix grain, corresponding to the ones marked as 1, 2 and 3, respectively, in (a) are also shown.

Table 1
Composition on the points shown in Fig. 3 derived from EDS spectra (at.%).

	O	Na	K	Li	Mn	Nb	Ta	Sb	Na/K
1	64.77	0.42	9.47	–	1.60	19.69	2.92	1.14	0.05
2	58.02	0.90	6.08	–	19.70	11.00	0.88	3.41	0.15
3	61.72	8.67	7.89	–	0.25	18.63	1.97	0.88	1.10
TTB[24] $Li_x(K_{0.78}Na_{0.22})_6(Nb_{0.86}Ta_{0.10}Sb_{0.04})_{10.9}O_{30}$	63.97	2.81	9.98	–	–	19. 99	2.32	0.92	0.28
$KNL–NTS_{nominal\ composition}$	60.00	10.40	8.80	0.80	0.00	17.2	2.00	0.80	1.18

marked as point 1 in Fig. 3a could be associated to the TTB secondary phase observed by XRD, since the composition measured by EDS is quite similar to that of $Li_x(K_{0.78}Na_{0.22})_6(Nb_{0.86}Ta_{0.10}Sb_{0.04})_{10.9}O_{30}$ tungsten bronze material [24], although our results reveal that the TTB phase grains present a K^+-rich composition. In addition, these grains show a high content of Mn^{2+} cations (see Fig. 3b), indicating that the grains of TTB phase are formed to accommodate the MnO excess that cannot be incorporated on the KLN–NTS lattice. The TTB phase showed a Na/K concentration ratio around 0.05, lower than the nominal ratio of 1.18. The abnormal grains are therefore accompanied by redistribution of the related elements (specially the A-site cations) that eventually precipitate and crystallize as a TTB secondary phase. The formation of the tungsten bronze structure requires a large diffusion of the atoms and therefore it is favored if the samples contain MnO.

Another interesting feature of the $(KNL)_{1-x}Mn_{x/2}$–NTS microstructure is the apparition of secondary re-crystallization in grain boundaries. These re-crystallized grains present laminar morphologies (point 2, Fig. 3a). The EDS analysis revealed that these regions have a composition rich in Mn^{2+} cations (see Fig. 3c), indicating again that the Mn^{2+}-excess cations should be accommodated through the formation of different secondary phases, TTB and secondary re-crystallization in grain boundaries.

Finally, the matrix grains (point 3, Fig. 3a) have the typical nominal composition with a Na/K concentration ratio around 1.10, slightly lower than the nominal ratio of 1.18 (see Fig. 3d). In addition, traces of Mn^{2+} can be observed on these grains by EDS, but the solubility of MnO in the perovskite lattice appears as limited. When the solubility limit is reached, the lattice cannot accommodate more MnO since it corresponds to B-site excess. Thus, the corresponding excess is directly compensated by the eviction of some Nb^{5+} ions, with formation of secondary phases.

3.3. Dielectric properties

Fig. 4a shows the temperature dependence of the relative permittivity, ε_r, and dielectric losses (at 100 kHz) in $(KNL)_{1-x}Mn_{x/2}$–NTS ceramics with different MnO amounts. The relative permittivity presents a maximum corresponding to the transition from the ferroelectric tetragonal phase to the paraelectric cubic phase at Curie temperature, T_c. As the MnO content increases, the relative permittivity at T_c decreases up to a minimum value of ~3650 for the ceramics with $x = 0.05$. A decrease of the Curie temperature T_c was also detected with increasing MnO substitution, suggesting that the Mn^{2+}-addition modify this phase transition temperature. This kind of behaviour has also been reported by other

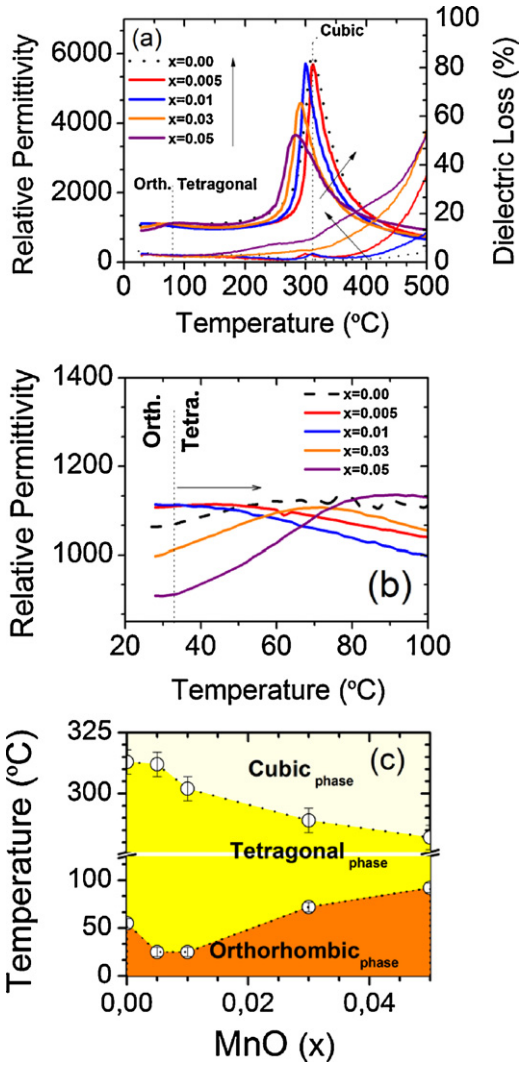

Fig. 4. (a) Temperature dependence of the relative permittivity, ε_r, and dielectric losses (at 100 kHz) for $(KNL)_{1-x}Mn_{x/2}$–NTS ceramics with different contents of MnO. In the part (b) temperature dependence of the relative permittivity at temperatures from 20 °C to 100 °C of the $(KNL)_{1-x}Mn_{x/2}$–NTS ceramics. The part (c) shows the evolution of the T_c and the phase transition temperatures from orthorhombic to tetragonal phase (T_{O-T}) of the $(KNL)_{1-x}Mn_{x/2}$–NTS ceramics with different contents in MnO. (The sensitivity of the phase transition temperatures, T_{O-T} and T_c, was estimated on ±5 °C.)

authors for Mn^{2+}-doped $(Na_{0.5}Bi_{0.5})_{1-x}Ba_xTiO_3$ [28]. Moreover, the addition of MnO produces a slight broadening of the transition peak, suggesting diffuse phase transition characteristic. This result means that the relaxor-type characteristics are more relevant for the ceramics with a high MnO content. The relaxor-type behaviour can be induced in many ways, such as microscopic compositional fluctuations, the merging of micro-domains into macro-domains, or a coupling of the order parameter and local disorder mode through the local strain. Mn^{2+} ions can incorporate into both A and B-sites of the perovskite structure, increasing then the disorder of the lattice. Therefore, the cation disorder in the perovskite unit cell should be one of the reasons for the appearance of relaxor-behaviour for the samples with a higher MnO content. As previously shown, this cation disorder should be related to the microscopic compositional fluctuations, which are intensified by the previously observed increase of abnormal grains and secondary TTB phase.

Close to room temperature, anomalous behaviour is observed in the dielectric response, Fig. 4b. This anomaly is identified by a weak maximum of the permittivity. It is well known that (K,Na)NbO_3 presents a phase transition from the orthorhombic to the tetragonal ferroelectric phases, O–T, close to ~200 °C [29]. It is also known that in (K,Na,Li)(Nb,Ta)O_3 ceramics the orthorhombic–tetragonal phase transition temperature decreases as a result of the Li^+ addition, which stabilizes the tetragonal phase [30]. As for the structural distortion observed by XRD, no change is observed for low MnO contents, while the O–T phase transition temperature is increased for $x \geq 0.03$, Fig. 4b. According to X-ray diffraction results, Fig. 1, this evolution in the T_{O-T} corresponds to a stabilization of the orthorhombic symmetry at room temperature.

Taking into account the previous results, a phase diagram has been proposed for $(KNL)_{1-x}Mn_{x/2}$–NTS ceramics, as shown in Fig. 4c. This phase diagram evidences that the ferroelectric phase transition (T_c) decreases monotonously with the MnO content. On the other hand, the orthorhombic to tetragonal (T_{O-T}) phase transition remains unaffected by the MnO addition up to $x = 0.01$, while higher Mn contents induce an increase of the phase transition temperature T_{O-T}. This indicates that, even though Mn^{2+} is entering in the KNL–NTS structure, as evidenced by the changes on the Curie temperature T_c, the T_{O-T} is not affected by this incorporation at low concentrations, but is highly modified for MnO contents higher than $x = 0.01$. This fact could indicate that Mn^{2+} incorporation on the KNL–NTS structure occurs in two phases: for low contents it enters primarily on the A-site of the perovskite lattice, while at high concentrations it simultaneously enters on the A and B-sites.

Fig. 5a and b represents the room temperature dielectric properties of $(KNL)_{1-x}Mn_{x/2}$–NTS unpoled ceramics at different frequencies. The Mn^{2+} addition globally induces a decrease of the relative permittivity (Fig. 5c), together with a slight increase of the dielectric losses (Fig. 5d), but all the ceramics present dielectric losses values lower than 4% at 1 kHz.

Furthermore, the dielectric constant for low MnO addition ($x \leq 0.01$) is higher than for the sample without MnO, Fig. 5c. The relative permittivity response shows a large range of frequency with stable dielectric constant, in contrast to the situation found for undoped sample which presents a slight dependency of the dielectric constant versus the frequency, Fig. 5a. The reduction on the relative permittivity is a favorable result for power applications since it will lower the capacitive effect of the piezoceramic actuators.

3.4. Piezoelectric properties

Fig. 6 presents the piezoelectric properties (d_{ij}) and mechanical quality factor (Q_m) as a function of the MnO content. As shown in this figure, the d_{33} and d_{31} values for the undoped ceramic were ~265 and ~105 pC/N, respectively. The d_{33} value decreases gradually up to a value of ~98 pC/N for the composition with the highest MnO content ($x = 0.05$). A similar but less pronounced evolution was observed for d_{31} coefficient.

A high Q_m value is desirable for resonant piezoelectric devices in order to suppress heat generation during the operation of the device [31,32]. In the literature, the Q_m values for undoped KNL–NTS are reported to be between 30 [32] and 65 [27]. When increasing MnO content, the Q_m factor was found to increase from 45 for samples without MnO up to 90 for $x = 0.03$, and further increase of Mn content does not produce any increment of this value. To sum up, the substitution of small amounts of cations modifies the dielectric and piezoelectric properties resulting in a reduction of the dielectric constant and of the piezoelectric activity, while the mechanical quality factor, Q_m, is increased.

3.5. Ferroelectric properties

Fig. 7a presents room temperature *P*–*E* hysteresis loops for $(KNL)_{1-x}Mn_{x/2}$–NTS ceramics. Well-saturated hysteresis loops

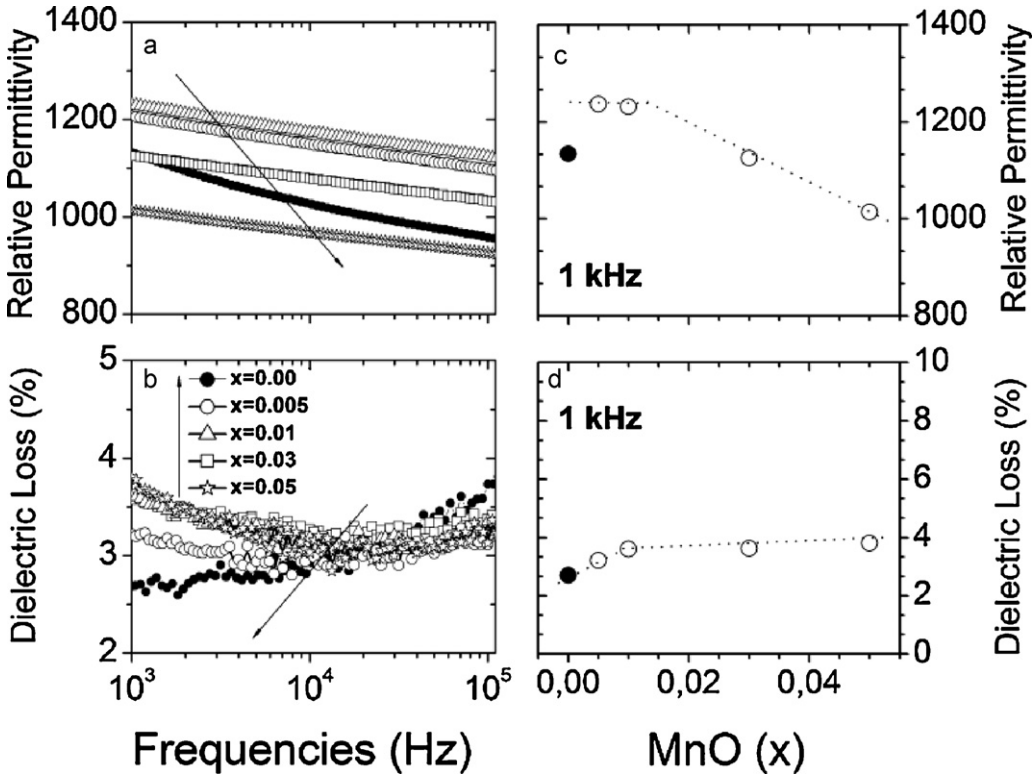

Fig. 5. (a) Relative permittivity and (b) dielectric losses as function of the frequency for $(KNL)_{1-x}Mn_{x/2}$–NTS ceramics with different MnO contents. The part (c) shows the evolution of the dielectric constant at 1 kHz in the unpoled ceramics. The part (d) shows the evolution of the dielectric losses at 1 kHz in the unpoled ceramics.

were clearly obtained in all samples. The remnant polarization, P_r, and coercive field, E_c, of the samples without MnO were previously found to be 18.2 μC/cm^2 and 15.8 kV/cm, respectively [33]. As for the structural evolution (XRD, phase transition temperatures, piezoelectric properties), two different ranges can be distinguished on the evolution of the remnant polarization (Fig. 7b): when a small amount of MnO was added ($x \leq 0.01$), P_r remains constant while E_c is increased up to 17 kV/cm. For higher x values ($x > 0.01$), the P_r values gradually decrease from ~18.2 to 8.2 μC/cm^2 while E_c is also decreased to ~10 kV/cm. The decrease in P_r suggests that the addition of MnO weakens the ferroelectricity of the ceramics. Similar weakening effects have also been reported for other modified KNN-systems, such as KNN–CuO [27].

The remnant polarization is an important macroscopic property of ferroelectric materials. Its magnitude, as evidenced from Fig. 7a, is related to the crystal structure of the material and modulated in a ceramic material by the microstructure. For ferroelectric materials,

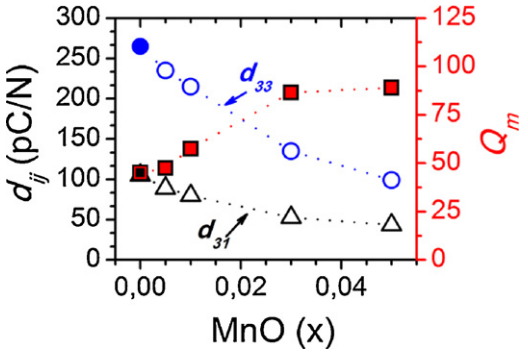

Fig. 6. Variations of the piezoelectric constants, d_{ij} and the planar mechanical quality, Q_m, with the amount of MnO in the $(KNL)_{1-x}Mn_{x/2}$–NTS ceramics (standard tolerance: piezoelectric constant ±5% (except for Q_m)).

a linear relationship has been proposed between the spontaneous polarization, P_s, and the ionic effective displacement, Δz_{eff}, of the active ferroelectric ion. Abrahams et al. [34] have suggested the following equation:

$$P_s \sim K(\Delta z_{eff}) \quad (2)$$

where $K = (258 \pm 9)$ μC/cm^{2}Å. Our previous results for KNL–NTS piezoelectric ceramics [35,36] revealed that (i) the best piezoelectric properties are obtained for the tetragonal symmetry and (ii) there is a linear correlation between the tetragonal distortion, c/a, and the piezoelectric properties. Then, a linear relation is expected to occur between spontaneous polarization, P_s, and the tetragonal distortion, c/a, for $(KNL)_{1-x}Mn_{x/2}$–NTS ceramics depending on the MnO content. As noticed here above (cf. structural characterization), two different point groups were used for XRD patterns refinement, corresponding to tetragonal and orthorhombic symmetries. In this situation and in order to be able to compare structural distortions for both symmetries, the true tetragonal distortion, c/a, was used for tetragonal samples, while a *pseudotetragonality* was calculated for orthorhombic samples using a normalized lattice parameter $a = (a_{ortho} + b_{ortho})/2$.

Using the experimental values of P_r in Eq. (2) and assuming that a proportionality is usually found between P_s and P_r, we also calculated Δz_{eff} values for the different samples under study; see Fig. 8a. We noticed that the highest value of effective displacement of the central ion (0.058 ± 0.002 Å) corresponds to the sample with the largest tetragonal distortion and $x = 0.005$.

Fig. 8b presents a simple schematic representation of the perovskite ABO_3 unit representing the structural evolution of the perovskite structure from tetragonal (point 1, Fig. 8a) to orthorhombic symmetry (point 4, Fig. 8a) with MnO substitution, illustrating the different ionic effective displacements (Δz_{eff}). In this schema, a larger tetragonal distortion implies a higher value of displacement of the central ion (B^{5+}) from its equilibrium position,

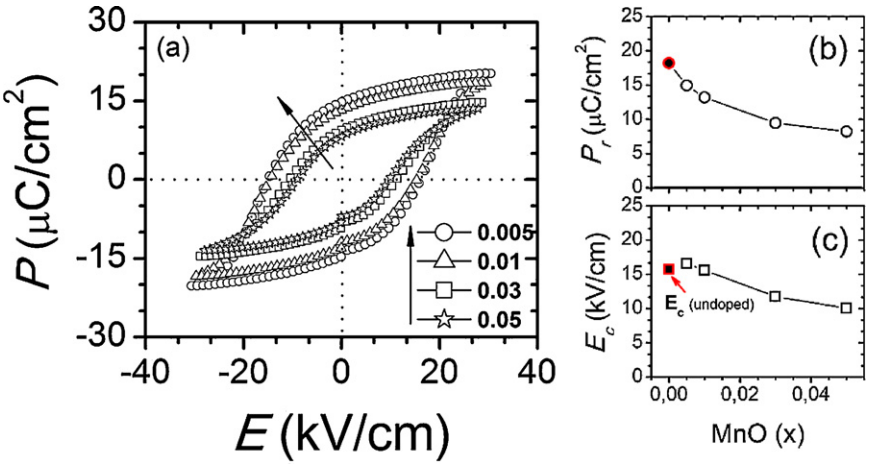

Fig. 7. (a) Polarization-field response of the for $(KNL)_{1-x}Mn_{x/2}$–NTS ceramics with different MnO contents. Effect of Mn^{2+} addition on (b) remnant polarization, P_r, and (c) coercive field, E_c, of $(KNL)_{1-x}Mn_{x/2}$–NTS ceramics.

Δz_{eff}. This displacement is illustrated in Fig. 8b as occurring along the *c* axis in the perovskite ABO_3 unit cell. Therefore, this structural modification, as it was observed by XRD, implies large changes in crystal structure and a modification of the spontaneous polarization, P_s. Thus, both P_s and Δz_{eff} are effectively correlated to the structural distortion, as demonstrated in Fig. 8a.

4. Discussion

As it has been discussed above in Section 1, the ionic radius of Mn^{2+} falls in the size range of A-site and B-site positions, and therefore Mn^{2+} ion could potentially substitute in either A or B-site. Indeed, for transition metal elements, the most probable position is the B-site from crystal-chemistry considerations, but the incorporation of a limited content of Mn^{2+} in A-site cannot be excluded. As noticed above, we selected a global formula, $(K_{0.44}Na_{0.52}Li_{0.04})_{(1-x)}Mn_{(x/2)}(Nb_{0.86}Ta_{0.10}Sb_{0.04})O_3$, which implies A-site deficiency. Consequently it can be suggested the following two equations using the Kröger–Vink's notation [37] which can describe the doping behaviour of Mn^{2+} in this system:

$$MnO \rightarrow Mn_A^{\bullet} + O_O + V'_A \quad (3)$$

$$2MnO \rightarrow 2Mn'''_B + 2O_O + 3V_O^{\bullet\bullet} \quad (4)$$

The first mechanism corresponds to the creation of A-site vacancies, V'_A, while the second one is associated to the occurrence of oxygen vacancies, $V_O^{\bullet\bullet}$. The A-site vacancies generally facilitate the movements of the ferroelectric domains and made the polarization switching easier [38]. Oxygen vacancies are unfavorable to polarization switching, because they imply pinning of the domain walls and thus lead to an increase of coercive field (hardening effect) and also to a reduction in permittivity, dielectric and mechanical losses.

Thus, the stabilization of piezoelectric properties at low doping levels is also thought as being associated with the Mn donor doping effects. When the amount of Mn is lower than 0.01, Mn^{2+} may occupy the A-sites (donor-type doping), substituting K^+, Na^+ and Li^+ ions, which causes a slack of the lattice and enhances the motion of 90° domains [39]. Coexistence of the motion of 90° and 180° domains leads to the stabilization of piezoelectric properties [33].

However, the solubility of MnO in the perovskite lattice seems to be rather limited: such limit would be around $x = 0.01$, as the TTB-like secondary phase start to be detected by XRD at this doping level (Fig. 1b). When the amount of Mn is higher than 0.01, the piezoelectric properties decrease while Q_m increases which is probably due to the fact that more Mn^{2+} ions will substitute B-site ions. Under this condition, Mn^{2+} ions exhibit some properties of acceptor type additives. When the amount of Mn^{2+} is over 0.01, Mn^{2+} ions are supersaturated in the lattice of KNL–NTS, and the excess Mn^{2+} ions accumulate in the grain boundaries and favor the formation of TTB secondary phase, as evidenced in Fig. 2c and d. The excess Mn^{2+}-ions replace some of the B-ions (Nb/Ta/Sb) which thus help to form the TTB phase. The replacement of the (Nb/Ta/Sb) ions in

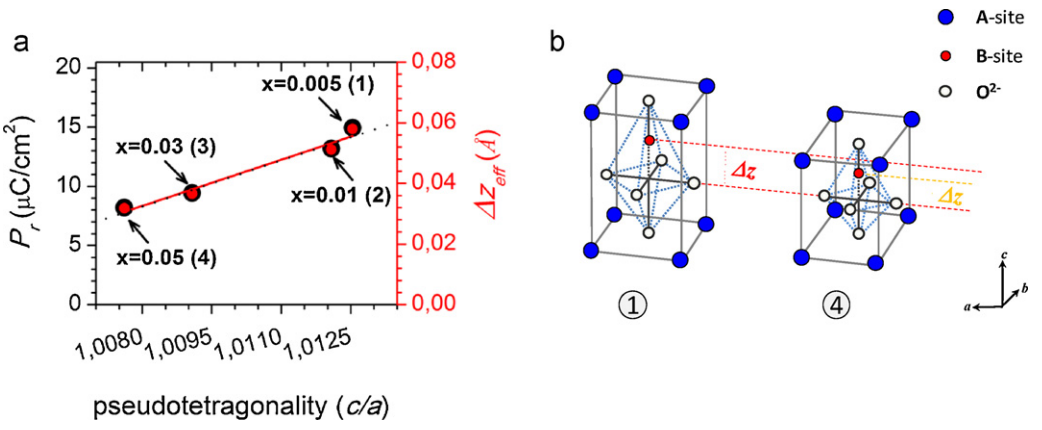

Fig. 8. (a) Evolution of the remnant polarization (P_r) and the ionic effective displacement (Δz_{eff}) as a function of the pseudotetragonality, for the $(KNL)_{1-x}Mn_{x/2}$–NTS ceramics. (b) Schematic representation of the perovskite ABO_3 unit cell for the different crystalline phases of the system at room temperature. The schematic representation shows the evolution structural of the perovskite phase from tetragonal symmetry (1) to orthorhombic symmetry (4), which illustrates the different ionic effective displacements (Δz_{eff}).

B-site by larger Mn^{2+} ions thus explains the reduction in the amplitude of the remnant polarization and in the piezoelectric properties [40,41], together with the increase of Q_m.

5. Conclusions

In summary, $(KNL)_{1-x}Mn_{x/2}$–NTS lead-free ceramics with interesting ferroelectric and piezoelectric properties have been developed by normal sintering. By adding a small amount of MnO to KNL–NTS, the crystalline structure is only slightly modified and the perovskite phase remains of tetragonal symmetry. On the other hand, for MnO doping levels $x \geq 0.01$ a secondary phase with tetragonal tungsten-bronze structure is observed by XRD, accompanied by a modification of the crystalline structure towards an orthorhombic symmetry. The addition of Mn^{2+} produces a linear decrease of the tetragonal–cubic phase transition temperature (T_c). This change is accompanied by an increase of the orthorhombic to tetragonal polymorphic phase transition temperature (T_{O-T}). Finally, a decrease of the piezoelectric coefficient is observed with the added quantity of MnO. This reduction is related to the increase of the T_{O-T} polymorphic phase transition temperature and thus to the stabilization of the orthorhombic symmetry at room temperature. However, it significantly improved the mechanical quality factor (Q_m) of these materials.

Acknowledgements

The authors express their thanks to the MICINN (Spain) project MAT 2010-21088-C03-01 and COST Action MP0904 SIMUFER network for their financial support. Dr. F. Rubio-Marcos is indebted to the "Conseil Regional du Limousin" for post-doctoral fellowship. Authors thank to C.A. Fernández-Godino for his assistance in the preparation of the compositions.

References

[1] EU Directive 2002/95; http://ec.europa.eu/environment/waste/weee/index_en.htm.
[2] T.R. Shrout, S.J. Zhang, J. Electroceram. 19 (2007) 113–126.
[3] M. Matsubara, T. Yamaguchi, W. Sakamoto, K. Kikuta, T. Yogo, S. Hirano, J. Am. Ceram. Soc. 88 (2005) 1190–1196.
[4] Y. Lee, J. Yoo, K. Lee, I. Kim, J. Song, Y.-W. Park, J. Alloys Compd. 506 (2010) 872–876.
[5] R. Zuo, J. Rödel, R. Chen, L. Li, J. Am. Ceram. Soc. 89 (2006) 2010–2015.
[6] F. Rubio-Marcos, M.G. Navarro-Rojero, J.J. Romero, J.F. Fernández, J. Eur. Ceram. Soc. 29 (2009) 3045–3052.
[7] P. Bomlai, P. Sinsap, S. Muensit, S.J. Milne, J. Am. Ceram. Soc. 91 (2008) 624–627.
[8] M. Kosec, D. Kolar, Mater. Res. Bull. 10 (1975) 335–339.
[9] R.-C. Chang, S.-Y. Chu, Y.-P. Wong, C.-S. Hong, H.-H. Huang, J. Alloys Compd. 456 (2008) 308–312.
[10] Y. Guo, K.-I. Kakimoto, H. Ohsato, Appl. Phys. Lett. 85 (2004) 4121.
[11] R. López-Juárez, F. González-García, J. Zárate-Medina, R. Escalona-González, S. Díaz de la Torre, M.-E. Villafuerte-Castrejóna, J. Alloys Compd. 509 (2011) 3837–3842.
[12] K.C. Singh, C. Jiten, R. Laishram, O.P. Thakur, D.K. Bhattacharya, J. Alloys Compd. 496 (2010) 717–722.
[13] R. López, F. González, M.E. Villafuerte-Castrejón, J. Eur. Ceram. Soc. 30 (2010) 1549–1553.
[14] Q. Zhang, B.-P. Zhan, H.-T. Li, P.-P. Shang, J. Alloys Compd. 490 (2010) 260–263.
[15] N. Jiang, B. Fang, J. Wu, Q.B. Du, J. Alloys Compd. 509 (2011) 2420–2424.
[16] H.Q. Wang, R.Z. Zuo, J. Fu, Y. Liu, J. Alloys Compd. 509 (2011) 936–994.
[17] Y. Saito, H. Takao, T. Tani, T. Nonoyama, K. Takatori, T. Homma, T. Nagaya, M. Nakamura, Nature (London) 432 (2004) 84–87.
[18] D.A. Ochoa, J.A. García, R. Pérez, V. Gomis, A. Albareda, F. Rubio-Marcos, J.F. Fernandez, J. Phys. D: Appl. Phys. 42 (2009) 025402.
[19] R.D. Shannon, Acta Crystallogr. A32 (1976) 751–767.
[20] F. Rubio-Marcos, P. Ochoa, J.F. Fernández, J. Eur. Ceram. Soc. 27 (2007) 4125–4129.
[21] http://www.ferroperm-piezo.com.
[22] J. Tanaka, Y. Onoda, M. Tsukioka, M. Shimazu, S. Ehara, Jpn. J. Appl. Phys. 21 (1981) 451–455.
[23] G. Feng, L. Liangliang, X. Bei, C. Xiao, D. Zhenqui, T. Changsheng, J. Alloys Compd. 509 (2011) 6049–6055.
[24] Y. Wang, D. Damjanovic, N. Klein, N. Setter, J. Am. Ceram. Soc. 91 (2008) 1962–1970.
[25] D. Lin, K.W. Kwok, H. Tian, H.W.L. Chan, J. Am. Ceram. Soc. 90 (2007) 1458–1462.
[26] Y. Zhen, J.-F. Li, J. Am. Ceram. Soc. 90 (2007) 3496–3502.
[27] N. Marandian Hagh, K. Kerman, B. Jadidian, A. Safari, J. Eur. Ceram. Soc. 29 (2009) 2325–27332.
[28] X.Y. Zhou, H.S. Gu, Y. Wang, W.Y. Li, T.S. Zhou, Mater. Lett. 59 (2005) 1649–1652.
[29] B. Jaffe, W.R. Cook, H. Jaffe, Piezoelectric Ceramics, Academic, London, 1971.
[30] E. Hollenstein, M. Davis, D. Damjanovic, N. Setter, Appl. Phys. Lett. 87 (2005) 182905.
[31] M. Matsubara, T. Yamaguchi, K. Kikuta, S. Hirano, Jpn. J. Appl. Phys. 43 (2004) 7159–7163.
[32] E. Li, H. Kakemoto, S. Wada, T. Tsurumi, IEEE Trans. Ultrason. Ferroelectr. Freq. Control 55 (2008) 980–987.
[33] F. Rubio-Marcos, J.J. Romero, D.A. Ochoa, J.E. García, R. Perez, J.F. Fernández, J. Am. Ceram. Soc. 93 (2010) 318–321.
[34] S.C. Abrahams, S.K. Kurtz, P.B. Jamieson, Phys. Rev. 172 (1968) 551.
[35] F. Rubio-Marcos, M.G. Navarro-Rojero, J.J. Romero, P. Marchet, J.F. Fernández, IEEE Trans. Ultrason. Ferroelectr. Freq. Control 56 (2009) 1835–1842.
[36] F. Rubio-Marcos, M.A. Bañares, J.J. Romero, J.F. Fernández, J. Raman Spectrosc. 42 (2011) 639–643.
[37] F.A. KrÖeger, Chemistry of Imperfect Crystals, North-Holland, Amsterdam, Netherlands, 1964.
[38] E.V. Ramana, S.V. Suryanarayana, T.B. Sankaram, Solid State Sci. 12 (2010) 956–962.
[39] P. Roy-Chowdhury, S.B. Deshpande, J. Mater. Sci. 22 (1987) 2209–2215.
[40] W.L. Zhong, Physics of Ferroelectrics, Science Press, Beijing, China, 1996, pp. 274–285.
[41] T. Kamiya, T. Suzuki, T. Tsurumi, M. Daimon, Jpn. J. Appl. Phys. 31 (1992) 3058–3060.